Proceedings of the ASME 2011 International Design Engineering Technical Conferences &
Computers and Information in Engineering Conference
IDETC/CIE 2011
August 28-31, 2011, Washington, DC, USA

DETC2011/MECH-48829

DELAYED CAR-FOLLOWING DYNAMICS FOR HUMAN AND ROBOTIC DRIVERS

Gábor Orosz[*]
Department of Mechanical Engineering
University of Michigan
Ann Arbor, Michigan 48109
Email: orosz@umich.edu

Jeff Moehlis
Francesco Bullo
Department or Mechanical Engineering
University of California
Santa Barbara, California 93106
Email: moehlis@engineeering.ucsb.edu
bullo@engineeering.ucsb.edu

ABSTRACT

A general class of car-following models is analyzed where the longitudinal acceleration of a vehicle is determined by a nonlinear function of the distance to the vehicle in front, their velocity difference, and the vehicle's own velocity. The driver's response to these stimuli includes the driver reaction time that appears as a time delay in governing differential equations. The linear stability of the uniform flow is analyzed for human-driven and computer-controlled (robotic) vehicles. It is shown that the stability conditions are equivalent when considering ring-road and platoon configurations. It is proven that time delays result in novel high-frequency oscillations that manifest themselves as short-wavelength traveling waves. The theoretical results are illustrated using an optimal velocity model where the nonlinear behavior is also revealed by numerical simulations. The results may lead to better understanding of multi-vehicle dynamics and allow one to design cooperative autonomous cruise control algorithms.

INTRODUCTION

Vehicular traffic is one of the most complex interconnected dynamical systems created by mankind. Each vehicle is controlled by a human operator (sometimes assisted by an on-board computer) who senses the environment (i.e., the motion of other vehicles, traffic signals and road conditions), makes decisions

based on the collected information and actuates the car accordingly. This process takes a finite amount time, known as the driver reaction time. The emergent dynamics of a traffic system, i.e., the time evolution of traffic patterns over large time and length scales, is determined by these delayed, nonlinear driver-to-driver and driver-to-infrastructure interactions. In this paper we focus our attention on the former one and study the corresponding car-following dynamics.

By now, a vast number of different car-following models have been constructed [1–3], but still no first principles have been established to guide the modeling procedure (if such principles exist at all). In many cases, authors have claimed that the developed model described traffic better than models prior to that point, and such claims were often justified by fitting the models to empirical data. This approach may easily lead to models capturing, but also missing, some essential characteristics and a model fit to one set of data may no longer be predictive when extrapolated to new sets of data. We believe that another way to conduct research in traffic can be by studying general classes of models and classifying their qualitative dynamical features when varying model parameters.

Of particular interest is the stability of the uniform traffic flow in which vehicles follow each other with the same velocity because this state is beneficial for traffic safety and throughput. The approaches taken to analyze this state are very different in the physics, applied mathematics and control engineering communities. To bridge the gap between these approaches, here we

---

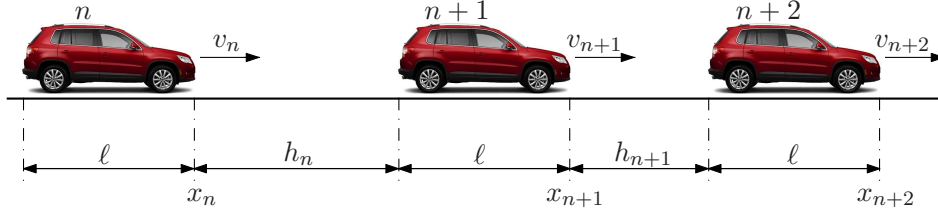[*]Address all correspondence to this author.

FIGURE 1. SEQUENCE OF CARS ON A SINGLE LANE SHOWING VEHICLES' POSITIONS, VELOCITIES, AND HEADWAYS.

calculate the flow stability by two different approaches and show that they lead to the same result for the considered general class of delayed car-following models when the number of vehicles is sufficiently large. (Such proof was presented for non-delayed models in the appendix of [3].) Both methods provide valuable insights into the dynamics underlying jam formation. In particular, apart from the location of the stability boundaries in parameter space, the frequencies of the arising oscillations and the wavelength of the developing traveling waves can be determined.

Although, this paper focuses on the linear stability of the uniform flow, we emphasize that car-following models are inherently nonlinear due to a fundamental speed-headway (or an equivalent flux-density) relation built into them. Since the detailed bifurcation analysis of car-following models goes beyond the scope of this paper we demonstrate the implications of the linear stability analysis on the nonlinear dynamics by numerical simulations.

MODELING CAR-FOLLOWING

In car-following models each driver-vehicle system is modelled by a set of differential equations that are coupled to other driver-vehicle systems based on the driver's responses to external stimuli. Fig. 1 shows a queue of vehicles on a single lane where vehicles have equal length ℓ. At time t, the position of the front bumper of the n-th car is denoted by $x_n(t)$, its velocity is $v_n(t) = \dot{x}_n(t)$ and the bumper-to-bumper distance to the vehicle in front (called the headway) is $h_n(t)$. It can be read from the figure that $h_n(t) = x_{n+1}(t) - x_n(t) - \ell$, which results in

$$\dot{h}_n(t) = v_{n+1}(t) - v_n(t), \qquad (1)$$

when differentiated with respect to time t. To complete the model, this equation has to be supplemented with a car-following rule, that is, the velocity or the acceleration has to be given as the function of stimuli that are usually the distance h_n, the velocity difference $\dot{h}_n$ and the vehicle's own velocity v_n. To represent the fact that the longitudinal dynamics of automobiles are controlled by varying the engine torque we choose a class of models where

the acceleration of vehicles is prescribed:

$$\dot{v}_n(t) = f\big(h_n(t-\tau), \dot{h}_n(t-\sigma), v_n(t-\kappa)\big). \qquad (2)$$

For simplicity, drivers with identical characteristics are considered. The delays τ, σ, κ represent driver reaction times to different stimuli (dead times required to process information and initiate action). To make the models more tractable, simple relations may be assumed between the different delays. There are three simplifications commonly used in the literature:

1. *Zero reaction times:* $\tau = \sigma = \kappa = 0$. This is usually justified by saying that dynamic models (2) may reproduce uniform flow as well as traveling waves for zero reaction time by varying some other characteristic times [4].
2. *'Human driver setup':* $\tau = \sigma > 0, \kappa = 0$. This setup represents that drivers react to the distance and to the velocity difference with (the same) delay but they are aware of their own velocity immediately [5,6].
3. *'Robotic driver setup':* $\tau = \sigma = \kappa > 0$. This setup is mainly used in the adaptive/automatic/autonomous cruise control (ACC) literature. The delay accounts for the time needed for sensing, computation and actuation in computer controlled vehicles [7,8].

Many other setups are also possible, for example, one may account for human memory effects by using distributed delays as in [9]. We remark that in the first case the system (1,2) consists of ordinary differential equations (ODEs) where the initial conditions are given by $h_n(0), v_n(0)$. In the latter cases, systems of delay differential equations (DDEs) are obtained where $h_n(t), v_n(t)$, $t \in [-\tau, 0]$ must be specified as initial conditions.

Determining the general properties of the multi-variable nonlinear function f in (2) is a difficult task. However, the model must be able to reproduce the uniform flow where both the velocities and the headways are time independent:

$$h_n(t) \equiv h^*, \quad \dot{h}_n(t) \equiv 0, \quad v_n(t) \equiv v^*. \qquad (3)$$

We also assume a functional relationship between the equilibrium headway h^* and the equilibrium velocity v^*, that is,

$$0 = f(h^*, 0, v^*) \quad \Rightarrow \quad v^* = V(h^*) \quad \Leftrightarrow \quad h^* = V^{-1}(v^*), \quad (4)$$

where V is assumed to have the following properties:

1. V is continuous and monotonically increasing (the more sparse traffic is, the faster drivers want to travel).
2. $V(h) \equiv 0$ for $h \leq h_{\text{stop}}$ (in very dense traffic, drivers intend to stop).
3. $V(h) \equiv v_{\text{max}}$ for large h (in very sparse traffic, drivers intend to drive with maximum speed – often called free flow).

This function is often called the range policy in the control literature [10]. Two examples are shown on the top panels in Fig. 2. The function on the left represents that between stopping and free-flow conditions, drivers intend to keep a constant time gap T_{gap} (also called time-headway), while the function on top right shows a scenario when the intended time gap changes with the distance/velocity.

One may define the equilibrium density and the flux as

$$\rho^* = \frac{1}{h^* + \ell}, \quad q^* = \rho^* v^* = \rho^* V(1/\rho^* - \ell) := Q(\rho^*). \quad (5)$$

This way the equilibrium speed-headway diagrams can be transformed into the equilibrium flux-density (fundamental) diagrams displayed at the bottom of Fig. 2. The rising part of the fundamental diagrams (that represents free flow) can be observed in empirical traffic data, collected by loop detectors, while usually a cloud appears instead of the decaying part (indicating unstable equilibria) [3]. Nevertheless the triangular fundamental diagram is often used for designing flow control strategies for ramp metering and variable speed limit control [11].

The equilibrium speed-density function (range policy) may be explicitly built into car-following models. The corresponding so-called optimal velocity (OV) model [4, 6, 10, 12] can be formulated as

$$f(h, \dot{h}, v) = \frac{1}{T}\big(V(h) - v\big) + b\dot{h}. \quad (6)$$

The first term corresponds to relaxation to a density dependent optimal velocity given by the increasing OV function V with a relaxation time T, while in the second, relative-velocity term we have $b \geq 0$. Despite its simplicity, the model (6) can reproduce qualitatively almost all kinds of traffic behavior.
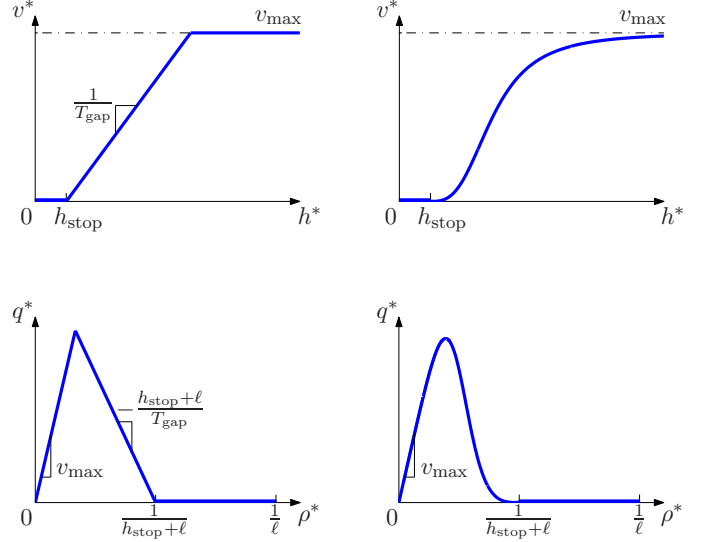
FIGURE 2. EQUILIBRIUM SPEED-HEADWAY DIAGRAMS $v^* = V(h^*)$ ARE SHOWN ON THE TOP, AND THE CORRESPONDING EQUILIBRIUM FLUX-DENSITY DIAGRAMS $q^* = Q(\rho^*)$ ARE DISPLAYED AT THE BOTTOM.

Another car-following model that satisfies the general conditions above is the intelligent driver model [7, 13]

$$f(h, \dot{h}, v) = a\left[1 - \left(\frac{v}{v_{\text{max}}}\right)^4 - \left(\frac{h_{\text{stop}} + vT_{\text{gap}} - \dot{h}v/\sqrt{4ab}}{h}\right)^2\right]. \quad (7)$$

In this model, a represents the maximum acceleration and b is the comfortable deceleration. Here the equilibrium speed-headway relationship is given by

$$h^* = V^{-1}(v^*) = \frac{h_{\text{stop}} + v^* T_{\text{gap}}}{\sqrt{1 - (v^*/v_{\text{max}})^4}}, \quad (8)$$

and the corresponding V is similar in shape to the functions in Fig. 2 – except that $V(h) < 0$ for $h \leq h_{\text{stop}}$. (However, the uniform flow is usually unstable here, and such a non-physical motion is rarely observed in simulations.) Notice that in (8) we have $V'(h_{\text{stop}}) = 1/T_{\text{gap}}$.

We emphasize that the reaction times τ, σ, κ (≈ 0.5–1.5 sec for human drivers, ≈ 0.1–0.2 sec for computer-controlled vehicles) are not equal to the time gap $T_{\text{gap}} \approx 1$–2 sec and these represent physically different features. They also differ from the relaxation time $T \approx 1$–10 sec that corresponds to the acceleration capabilities of vehicles.

There are two common vehicle configurations that allow one to characterize the stable and unstable motions that may give the skeleton of traffic dynamics.

1. *Ring-road configuration:* N vehicles are placed on a ring of length $L + N\ell$ (yielding $h^* = L/N$ and the periodic boundary condition $x_{N+1} = x_1$). Usually, the large N limit is taken: $N \to \infty$ such that L/N is kept constant. This configuration has been studied experimentally in [14].

2. *Platoon configuration:* $N + 1$ vehicles are placed on a road of infinite length and the motion of the leader ($N + 1$-st vehicle) is assigned – e.g., in equilibrium it travels with v^*. The system is viewed as an input (v_{N+1}) output (v_1) system with a chain of N nonlinear integrators. ACCs are usually designed using this configuration [15].

Notice that in the first approach, the key parameter is the equilibrium headway h^*, while in the second approach, it is the equilibrium velocity v^*. However, these quantities are linked by (4). We will show in the next section that the conditions for the linear stability of the uniform flow are equivalent for the two configurations in the large N limit. In this paper we use $N = 33$ when drawing stability charts, which is small enough to keep the illustrations readable but is large enough to represent the large N limit.

LINEAR STABILITY ANALYSIS

In this section we study the linear stability of the uniform flow for different delay setups using both the ring-road and the platoon configurations. Linearizing the system (1,2) about the equilibrium (3) and defining the perturbations $s_n(t) = h_n(t) - h^*$, $w_n(t) = v_n(t) - v^*$ one obtains

$$
\begin{aligned}
\dot{s}_n(t) &= w_{n+1}(t) - w_n(t), \\
\dot{w}_n(t) &= F s_n(t - \tau) + G \dot{s}_n(t - \sigma) - H w_n(t - \kappa),
\end{aligned} \tag{9}
$$

where the coefficients

$$
F = \partial_h f(h^*, 0, v^*), \quad G = \partial_{\dot{h}} f(h^*, 0, v^*), \quad H = -\partial_v f(h^*, 0, v^*) \tag{10}
$$

are assumed to be positive to obtain physically realistic driver behavior, i.e., drivers intend to decrease perturbations.

Ring-road and platoon configurations require different methods to analyze the stability. In the former case the system is autonomous and trial solutions $\sim e^{\lambda t}$, $\lambda \in \mathbb{C}$ may be used (which is equivalent to performing a Laplace transformation in time.) This leads to a $2N$-th order characteristic equation for λ. To obtain asymptotically stable uniform flow one needs to ensure that all characteristic roots are in the left-half complex plane, that is, $\mathrm{Re}(\lambda) < 0$ for all λ [6, 16].

Platoons are driven by the leader ($N + 1$-st vehicle). Here to obtain stable uniform flow, one must ensure that perturbations decay as they propagate upstream along the chain of vehicles.

At the linear level this can be addressed by studying the transfer function that links the Laplace transforms of w_{n+1} and w_n: if the magnitude of the transfer function is smaller than 1 for all excitation frequencies then the uniform flow is stable. This property is often called string stability in the literature [10, 15]. In the following subsections we determine these stability conditions for different delay setups.

Case 1 – Zero reaction time: $\tau = \sigma = \kappa = 0$

This case has already been reported in [3], but we review the results since it allows us to establish the framework that will be used in the forthcoming cases.

Considering the ring-road configuration, substituting the second equation to the first one in (9), and assuming the trial solution $s_n = \eta_n e^{\lambda t}$, $w_n = \xi_n e^{\lambda t}$, $\lambda, \eta_n, \xi_n \in \mathbb{C}$, one may obtain the characteristic equation

$$
(\lambda^2 + (G + H)\lambda + F)^N = (G\lambda + F)^N. \tag{11}
$$

Taking the Nth root of both sides, substituting $\lambda = i\omega$, $\omega \in \mathbb{R}_{\geq 0}$, separating the real and imaginary parts, and using trigonometrical identities, one may determine that the stability changes via Hopf bifurcations at

$$
\frac{F}{H^2} = \frac{1}{2}\left(2\frac{G}{H} + 1\right)\left[1 + \left(2\frac{G}{H} + 1\right)\tan^2\left(\frac{k\pi}{N}\right)\right], \tag{12}
$$

with angular frequency

$$
\frac{\omega}{H} = \left(2\frac{G}{H} + 1\right)\tan\left(\frac{k\pi}{N}\right), \tag{13}
$$

where $k = 1, \ldots, N - 1$ is a discrete wavenumber. The corresponding spatial wavelength is $\Lambda_+ = (L + N\ell)/k$ for $k \leq N/2$ and $\Lambda_- = (L + N\ell)/(N - k)$ for $k > N/2$; i.e., the same spatial pattern arises for wavenumbers k and $N - k$.

Note that for the physically realistic $F, G, H > 0$ parameter regime only the wavenumbers $k \leq N/2$ are admissible. Also note that the dimensionless parameters $F/H^2, G/H$ depend on the equilibrium h^*, v^*. It can also be shown that when crossing the above stability boundaries by increasing F, the pair of complex conjugate characteristic roots $\pm i\omega$ crosses the imaginary axis from left to right, i.e. the system becomes 'more unstable'. Since F/H^2 is an increasing function of k for $k < N/2$ (c.f., (12)), the stability loss occurs for the lowest wave-number $k = 1$. In the large N limit, we have $\frac{k\pi}{N} \to 0$ and so the stability condition becomes

$$
\frac{F}{H^2} < \frac{1}{2}\left(2\frac{G}{H} + 1\right), \tag{14}
$$

with frequency $\omega \to 0$. Note that for $\lambda = \mathrm{i}\omega$ one may calculate the eigenvector components $\xi_n = \mathrm{e}^{\mathrm{i}\frac{2k\pi}{N}n}$, so

$$w_n(t) = v_{\mathrm{amp}}\,\mathrm{Re}\big(\xi_n \mathrm{e}^{\mathrm{i}\omega t}\big) = v_{\mathrm{amp}}\cos\big(\tfrac{2k\pi}{N}n + \omega t\big), \qquad (15)$$

which shows that the oscillations manifest themselves as traveling waves (propagating upstream). When nonlinearities are added to the system the small-amplitude nonlinear oscillations can be written in the above form and the amplitude v_{amp} can be determined by normal form calculations [12, 16].

For the platoon configuration one can focus on the relationship between the velocity perturbations w_n and w_{n+1} in (9), and define the state, output, and input as $\mathbf{x} = [s_n, w_n]^T$, $y = w_n$, and $u = w_{n+1}$. That is, for zero delays (9) can be rewritten as

$$\dot{\mathbf{x}} = \mathbf{A}\mathbf{x} + \mathbf{B}u, \qquad\qquad y = \mathbf{C}\mathbf{x} + \mathbf{D}u,$$
$$\mathbf{A} = \begin{bmatrix} 0 & -1 \\ F & -(G+H) \end{bmatrix}, \quad \mathbf{B} = \begin{bmatrix} 1 \\ G \end{bmatrix}, \quad \mathbf{C} = \begin{bmatrix} 0 & 1 \end{bmatrix}, \quad \mathbf{D} = \begin{bmatrix} 0 \end{bmatrix}. \tag{16}$$

The corresponding transfer function becomes

$$\Gamma(\lambda) = \frac{\gamma_n(\lambda)}{\gamma_{n+1}(\lambda)} = \mathbf{C}(\lambda\mathbf{I} - \mathbf{A})^{-1}\mathbf{B} + \mathbf{D} = \frac{G\lambda + F}{\lambda^2 + (G+H)\lambda + F}, \tag{17}$$

where $\gamma_n(\lambda)$ is the Laplace transform of $w_n(t)$. Here, one may study the stability of the controller: the poles of $\Gamma(\lambda)$ have to be on the left half complex plane which is ensured by $F, G, H > 0$. On the other hand, to ensure the stability of the uniform flow (i.e., string stability), the inequality $|\Gamma(\mathrm{i}\omega)| < 1$ needs to be satisfied for all $\omega \in \mathbb{R}_{\geq 0}$, which results in the condition

$$\frac{F}{H^2} < \frac{1}{2}\Big(2\frac{G}{H} + 1\Big) + \frac{1}{2}\frac{\omega^2}{H^2}. \tag{18}$$

The right-hand side is minimal for $\omega \to 0$, yielding (14) as a condition for string stability. Notice that substituting the dispersion relation (13) into (12) results in (18), showing that the different approaches are equivalent.

Case 2 – Human-driver setup: $\tau = \sigma > 0, \kappa = 0$

Since $\tau > 0$ one may rescale the time as $\tilde{t} = t/\tau$ and define the non-dimensional characteristic roots $\tilde{\lambda} = \lambda\tau$ and frequencies $\tilde{\omega} = \omega\tau$. We remark that one may obtain the stability boundaries without this rescaling but the formulae may become more complicated.

For the ring-road configuration the characteristic equation becomes

$$\big(\tilde{\lambda}^2 + \tau H\tilde{\lambda} + (\tau G\tilde{\lambda} + \tau^2 F)\mathrm{e}^{-\tilde{\lambda}}\big)^N = \big((\tau G\tilde{\lambda} + \tau^2 F)\mathrm{e}^{-\tilde{\lambda}}\big)^N. \tag{19}$$

One may substitute $\tilde{\lambda} = \mathrm{i}\tilde{\omega}$, $\tilde{\omega} \in \mathbb{R}_{\geq 0}$ and separate the real and imaginary parts, but due to the exponential terms it is not possible to eliminate $\tilde{\omega}$. Instead the Hopf bifurcation curves are given in the parametric form

$$\frac{F}{H^2} = \frac{\big(2\frac{G}{H}\sin\big(\frac{k\pi}{N}\big) - \sin\big(\tilde{\omega} - \frac{k\pi}{N}\big)\big)\big(1 - 2\frac{G}{H}\sin\big(\frac{k\pi}{N}\big)\sin\big(\tilde{\omega} - \frac{k\pi}{N}\big)\big)}{2\sin\big(\frac{k\pi}{N}\big)\cos^2\big(\tilde{\omega} - \frac{k\pi}{N}\big)},$$
$$\tau H = \frac{\tilde{\omega}\cos\big(\tilde{\omega} - \frac{k\pi}{N}\big)}{2\frac{G}{H}\sin\big(\frac{k\pi}{N}\big) - \sin\big(\tilde{\omega} - \frac{k\pi}{N}\big)}, \tag{20}$$

which are shown in the top row of Fig. 3. Red arrows indicate the increase of the wavenumber k from 1 to $N/2$ (blue curves) and its decrease from $N-1$ to $N/2$ (green curves), that is, the spatial wavelength decreases from $L + N\ell$ to $2(L/N + \ell)$ in both cases. In the left panels the curves are ordered such that the stability boundary is given by the lowest wavenumber $k = 1$, that is, low-wavelength low-frequency oscillations are expected to appear when the stability is lost (as for the zero-delay case). In contrast, in the right panels, curves intersect each other and high-frequency short-wavelength oscillations are expected for sufficiently large delay. This behavior can be explained by the fact that for

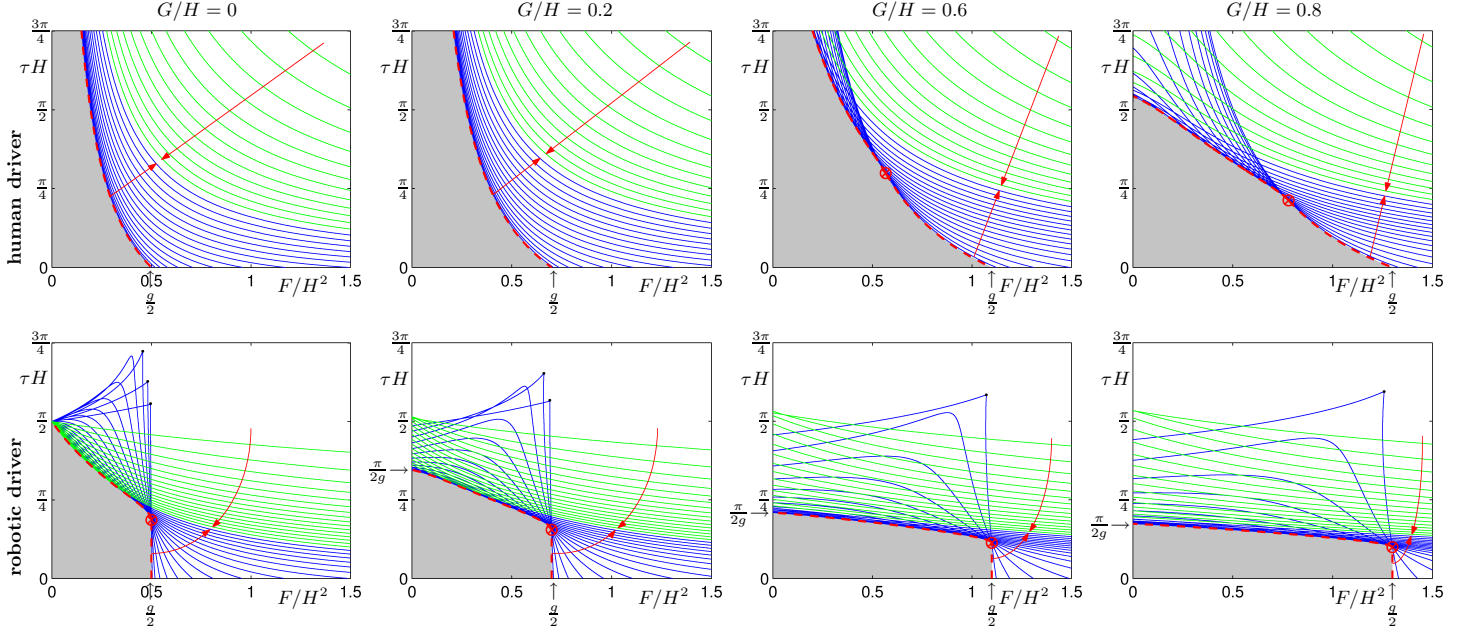$$\frac{G}{H} > \frac{1}{2\sin\big(\frac{k\pi}{N}\big)}, \tag{21}$$

the curves intersect the vertical axis at

$$\tau H\big|_{F=0} = \frac{\arcsin\Big\{\big[2\frac{G}{H}\sin\big(\frac{k\pi}{N}\big)\big]^{-1}\Big\} + \frac{k\pi}{N}}{\sqrt{4\frac{G^2}{H^2}\sin^2\big(\frac{k\pi}{N}\big) - 1}}, \tag{22}$$

which is a decreasing function of $\frac{k\pi}{N}$ on the interval $[0, \pi]$. That is, curves belonging to higher wavenumbers cross the vertical axis at smaller values of delay. Notice that according to (21) no curves intersect the vertical axis unless $G/H > 1/2$.

For the platoon configuration the transfer function becomes

$$\Gamma(\tilde{\lambda}) = \frac{(\tau G\tilde{\lambda} + \tau^2 F)\mathrm{e}^{-\tilde{\lambda}}}{\tilde{\lambda}^2 + \tau H\tilde{\lambda} + (\tau G\tilde{\lambda} + \tau^2 F)\mathrm{e}^{-\tilde{\lambda}}}, \tag{23}$$

5

FIGURE 3.   STABILITY DIAGRAMS FOR THE LINEARIZED MODEL (2) FOR HUMAN (TOP) AND ROBOTIC (BOTTOM) DRIVERS. THE STABLE REGIONS ARE SHADED AND HOPF BIFURCATIONS TAKE PLACE WHEN CROSSING THE BLUE AND GREEN CURVES GIVEN BY (20) AND (28). RED ARROWS SHOW THE CHANGE OF THE DISCRETE WAVELENGTH FROM $L + N\ell$ TO $2(L/N + \ell)$. THE NOTATION $g = 2\frac{G}{H} + 1$ IS USED; C.F. (14). THE THICK RED DASHED ENVELOPES CORRESPOND TO THE STRING STABILITY BOUNDARIES (25) AND (32), WHILE RED CROSSES SEPARATE THE LOW- AND HIGH- FREQUENCY SECTIONS.

and the condition $|\Gamma(i\tilde{\omega})| < 1$ leads to

$$
\begin{aligned}
P(\tilde{\omega}) = &\frac{1}{2}\Big(\frac{\tilde{\omega}^2}{\tau^2 H^2} + 1\Big) - \Big(\frac{F}{H^2} - \frac{G}{H}\Big)\cos\tilde{\omega} \\
&- \frac{\tau H}{\tilde{\omega}}\Big(\frac{F}{H^2} + \frac{G}{H}\frac{\tilde{\omega}^2}{\tau^2 H^2}\Big)\sin\tilde{\omega} > 0\,.
\end{aligned}
\tag{24}
$$

This is clearly satisfied if the minimum of the function $P(\tilde{\omega})$ is positive. Although, this minimum cannot be determined in closed form, one may differentiate the above formula and find the stability boundary by setting $P(\tilde{\omega}) = 0$, $\frac{\mathrm{d}}{\mathrm{d}\tilde{\omega}}P(\tilde{\omega}) = 0$ which leads to

$$
\begin{aligned}
&\frac{F}{H^2} = \frac{\frac{1}{2}\Big(\frac{\tilde{\omega}^2}{\tau^2 H^2} + 1\Big) + \frac{G}{H}\Big(\cos\tilde{\omega} - \frac{\tilde{\omega}}{\tau H}\sin\tilde{\omega}\Big)}{\cos\tilde{\omega} + \frac{\tau H}{\tilde{\omega}}\sin\tilde{\omega}}\,, \\
&\sum_{j=0}^{3} a_j\Big(\frac{\tau H}{\tilde{\omega}}\Big)^j = 0\,, \\
&a_0 = \frac{1}{2}\tilde{\omega}\sin\tilde{\omega} + \cos\tilde{\omega}\,, \\
&a_1 = \frac{1}{2}(3\sin\tilde{\omega} - \tilde{\omega}\cos\tilde{\omega}) - \frac{G}{H}(\sin\tilde{\omega}\cos\tilde{\omega} + \tilde{\omega})\,, \\
&a_2 = \frac{1}{2}\sin\tilde{\omega}\Big(\tilde{\omega} - 4\frac{G}{H}\sin\tilde{\omega}\Big)\,, \\
&a_3 = \frac{1}{2}(\sin\tilde{\omega} - \tilde{\omega}\cos\tilde{\omega}) + \frac{G}{H}(\sin\tilde{\omega}\cos\tilde{\omega} - \tilde{\omega})\,.
\end{aligned}
\tag{25}
$$

Solving the second equation one obtains τH as a function of $\tilde{\omega}$ and G/H, and the smallest (positive real) root can be substituted into the first equation. This way the string stability curve is obtained in a parametric form in the $(F/H^2, \tau H)$ plane. Indeed, the corresponding thick red dashed curve envelopes of the Hopf curves as shown by the upper row in Fig. 3. This proves that the two approaches used for determining the linear stability of the uniform flow give equivalent results.

When considering the limit $\tilde{\omega} \to 0$, equation (25) leads to

$$
\begin{aligned}
&\frac{F}{H^2} = \frac{1}{2}\Big(2\frac{G}{H} + 1\Big)\frac{1}{\tau H + 1}\,, \\
&(\tau H)^3\frac{1}{2}\Big(4\frac{G}{H} - 1\Big) + (\tau H)^2\frac{1}{2}\Big(4\frac{G}{H} - 1\Big) + \tau H\Big(2\frac{G}{H} - 1\Big) = 1\,,
\end{aligned}
\tag{26}
$$

where the second equation have a unique positive real solution for τH if and only if $G/H > 1/4$. In fact for $G/H < 1/4$ the string stability boundary is given by the first equation of (26) with $\tilde{\omega} \to 0$ (left panels, top row, Fig. 3), while for $G/H > 1/4$ this only gives the lower section of the curve and the upper section is given by (25) with $\tilde{\omega} > 0$ (right panels, top row, Fig. 3). The low-frequency and high-frequency sections are separated by a red cross that moves down and to the right when G is increased. Furthermore, considering $F = 0$ in the first equation of (25) one

6

may obtain $\tau H|_{F=0}$ and show that this only takes a finite value if $G/H > 1/2$. In summary, not only the boundaries but also the frequencies of arising oscillations are matched for the ring-road and platoon configurations.

Case 3 – Robotic-driver setup: $\tau = \sigma = \kappa > 0$

For the circular-road configuration the characteristic equation becomes

$$\left(\tilde{\lambda}^2 e^{\tilde{\lambda}} + \tau(G+H)\tilde{\lambda} + \tau^2 F\right)^N = \left(\tau G \tilde{\lambda} + \tau^2 F\right)^N, \qquad (27)$$

which results in the Hopf bifurcation curves

$$\frac{F}{H^2} = \frac{\left(2\frac{G}{H}+1\right)\left[\cos\left(\frac{k\pi}{N}\right) - \left(2\frac{G}{H}+1\right)\sin\left(\frac{k\pi}{N}\right)\tan\left(\tilde{\omega}-\frac{k\pi}{N}\right)\right]}{2\cos\left(\tilde{\omega}-\frac{k\pi}{N}\right)},$$

$$\tau H = \frac{\tilde{\omega}\cos\left(\tilde{\omega}-\frac{k\pi}{N}\right)}{\left(2\frac{G}{H}+1\right)\sin\left(\frac{k\pi}{N}\right)}, \qquad (28)$$

that are shown at the bottom in Fig. 3. Now for any value of G/H the curves cross the vertical axis at

$$\tau H|_{F=0} = \frac{\arctan\left\{\left[\left(2\frac{G}{H}+1\right)\tan\left(\frac{k\pi}{N}\right)\right]^{-1}\right\} + \frac{k\pi}{N}}{\sqrt{\left(2\frac{G}{H}+1\right)^2\sin^2\left(\frac{k\pi}{N}\right) + \cos^2\left(\frac{k\pi}{N}\right)}}, \qquad (29)$$

which is again a decreasing function of $\frac{k\pi}{N}$ on the interval $[0,\pi]$. (For $k = N/2$, we have $\tau H|_{F=0} = \pi/2/(2G/H+1)$, which takes the value $\pi/2$ for $G = 0$ and approaches 0 when G increases as indicated in the figure.) This leads to multiple crossings between the stability curves of different wavenumbers.

There also exists a critical "point" where large large number of intersections occur and the behavior changes radically. Below this, long-wavelength low-frequency oscillations arise when stability is lost by increasing the gain F, while above the critical point short-wavelength high-frequency oscillations are expected. Furthermore, a trade-off may be observed when comparing the panels for different values of G/H: increasing G the width of the stable regime increases but its height decreases, i.e., the system tolerates smaller delays.

For the platoon configuration the transfer function becomes

$$\Gamma(\tilde{\lambda}) = \frac{\tau G \tilde{\lambda} + \tau^2 F}{\tilde{\lambda}^2 e^{\tilde{\lambda}} + \tau(G+H)\tilde{\lambda} + \tau^2 F}, \qquad (30)$$

which yields the stability condition

$$Q(\tilde{\omega}) = \frac{1}{2}\frac{\tilde{\omega}^2}{\tau^2 H^2} + \frac{1}{2}\left(2\frac{G}{H}+1\right) - \frac{F}{H^2}\cos\tilde{\omega}$$
$$- \left(\frac{G}{H}+1\right)\frac{\tilde{\omega}}{\tau H}\sin\tilde{\omega} > 0. \qquad (31)$$

Considering $Q(\tilde{\omega}) = 0$, $\frac{\mathrm{d}}{\mathrm{d}\tilde{\omega}}Q(\tilde{\omega}) = 0$ one may obtain

$$\frac{F}{H^2} = \frac{1}{2}\left(2\frac{G}{H}+1\right)\cos\tilde{\omega} + \frac{1}{\tau H}\left(\frac{G}{H}+1\right)\sin^2\tilde{\omega}$$
$$+ \frac{1}{2}\frac{\tilde{\omega}}{\tau^2 H^2}\left(\tilde{\omega}\cos\tilde{\omega} - 2\sin\tilde{\omega}\right),$$
$$\sum_{j=0}^{2} b_j(\tau H)^j = 0, \qquad (32)$$
$$b_0 = \frac{1}{2}\tilde{\omega}\left(\tilde{\omega}\sin\tilde{\omega} + 2\cos\tilde{\omega}\right),$$
$$b_1 = -\left(\frac{G}{H}+1\right)\left(\sin\tilde{\omega}\cos\tilde{\omega} + \tilde{\omega}\right),$$
$$b_2 = \frac{1}{2}\left(2\frac{G}{H}+1\right)\sin\tilde{\omega},$$

where the second equation may be solved for τH and the smaller (positive real) root can be substituted into the first equation. Again the corresponding parametric curve gives the envelope of the Hopf curves as shown by the thick dashed curve in Fig. 3. That is the two different stability calculations indeed result in the same stability condition.

In this case, taking the limit $\tilde{\omega} \to 0$, equation (32) yields

$$\frac{F}{H^2} = \frac{1}{2}\left(2\frac{G}{H}+1\right),$$
$$(\tau H)^2\frac{1}{4}\left(2\frac{G}{H}+1\right) - \tau H\left(\frac{G}{H}+1\right) + \frac{1}{2} = 0. \qquad (33)$$

Here the first equation gives the string stability boundary on the interval $\tau H \in [0,\theta]$, where θ is the smaller solution of the second equation. This is depicted by the vertical section of the red dashed curve in Fig. 3 (bottom row). The critical point $(\tau H, F/H^2) = (G/H + 1/2, \theta)$ is marked by red a cross that moves down and to the right as G is increased. We have $\gamma = 2 - \sqrt{2}$ for $G = 0$ while θ approaches 0 for large G. The section of the red dashed curve above the cross is given by (32) for $\tilde{\omega} > 0$ that is high-frequency oscillations are expected for sufficiently large delay for any value of G corresponding to the results obtained from the ring-road configuration.
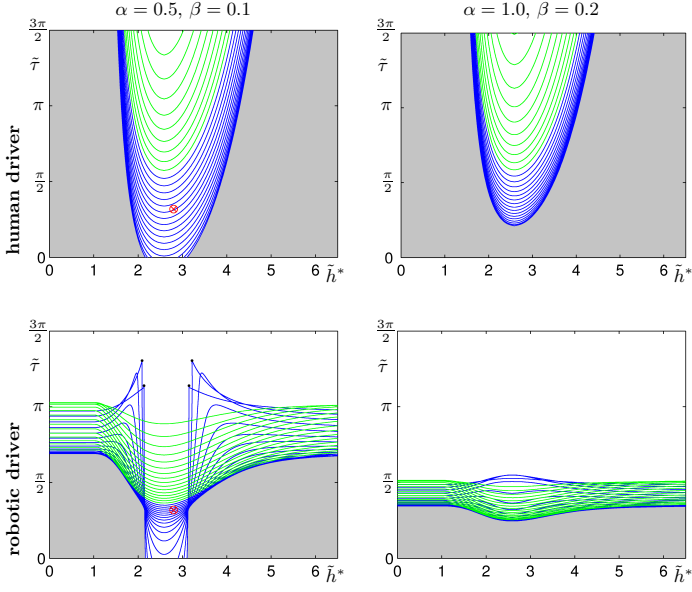
FIGURE 4. STABILITY DIAGRAMS FOR THE OPTIMAL VE-LOCITY MODEL (35). THE PARAMETER CHOICES CORRE-SPOND TO THE SECOND COLUMN IN Fig. 3.

FIGURE 5. NUMERICAL SIMULATIONS CORRESPONDING TO THE MARKS IN THE LEFT PANELS OF Fig. 4. NOTICE THAT THE APPEARING CHARACTERISTIC WAVELENGTHS ARE VERY DIFFERENT IN THE TWO CASES.

Stability of the optimal velocity model with delay

In this section we apply the above stability criteria to the optimal velocity model (6) where

$$F = \frac{V'(h^*)}{T}, \ G = b, \ H = \frac{1}{T}, \quad \Rightarrow \quad \frac{F}{H^2} = V'(h^*)T, \ \frac{G}{H} = bT.$$
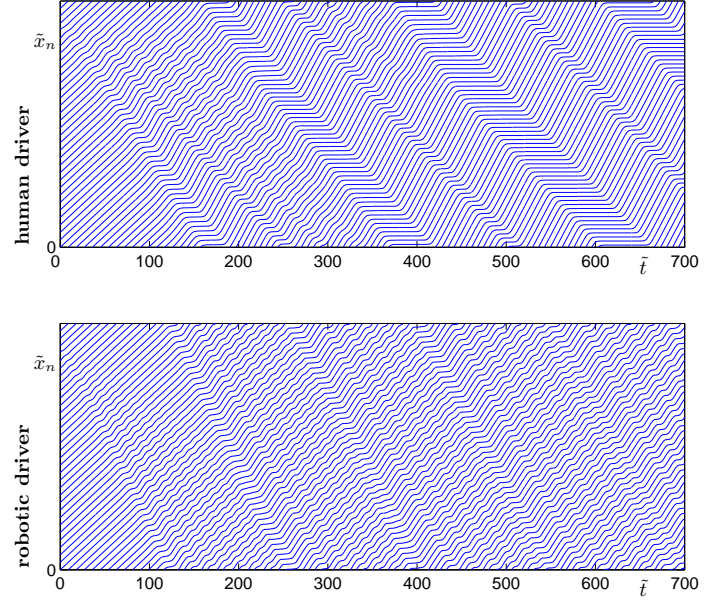(34)

To decrease the number of parameters we rescale distances by the desired stopping distance h_{stop} (that is, $\tilde{h} = h/h_{\text{stop}}$) and rescale velocities by the desired maximum velocity v_{max} (that is, $\tilde{v} = v/v_{\text{max}}$). Consequently, time is rescaled as $\tilde{t} = tv_{\text{max}}/h_{\text{stop}}$. The rescaled OV model can be written as

$$\tilde{f}(\tilde{h}, \dot{\tilde{h}}, \tilde{v}) = \alpha \big(\widetilde{V}(\tilde{h}) - \tilde{v} \big) + \beta \dot{\tilde{h}},$$
(35)

where the rescaled OV function

$$\widetilde{V}(\tilde{h}) = \begin{cases} 0, & \text{if} \quad \tilde{h} \in [0,1], \\ \dfrac{((\tilde{h}-1)/d)^3}{1+((\tilde{h}-1)/d)^3}, & \text{if} \quad \tilde{h} \in [1,\infty), \end{cases}$$
(36)

is used, in which the constant d describes how much the OV function is stretched to the right of $\tilde{h} = 1$. Here we use $d = 2$; c.f. top right panel in Fig. 2. Furthermore, we will use the

nondimensional parameters

$$\alpha = \frac{h_{\text{stop}}}{T v_{\text{max}}}, \quad \beta = \frac{b h_{\text{stop}}}{v_{\text{max}}}, \quad \tilde{\tau} = \frac{\tau v_{\text{max}}}{h_{\text{stop}}}, \quad \tilde{h}^* = \frac{h^*}{h_{\text{stop}}}. \quad (37)$$

Also, formulae (34,37) lead to

$$\frac{F}{H^2} = \widetilde{V}'(\tilde{h}^*)\alpha, \qquad \frac{G}{H} = \frac{\beta}{\alpha}.$$
(38)

Here we vary α and consider $\beta/\alpha = 0.2$, which corresponds to the second column of Fig. 3. Using (36) one may transform these into the diagrams shown in Fig. 4, where the stability curves are plotted in the $(\tilde{h}^*, \tilde{\tau})$ plane (for different values of α). It can be seen that for human-driven vehicles increasing α is beneficial for stability. However, it can be shown that there exists a critical delay above which instability cannot be eliminated by increasing α. On the other hand, for robotic vehicles increasing α leads to a trade-off: the unstable domain disappears for small delays but in the meantime the maximum tolerable delay is decreasing.

NONLINEAR BEHAVIOR

In this section we demonstrate by numerical simulation that the oscillations of different wavelengths that are suggested by the linear stability analysis, do appear in the nonlinear system. In particular, we marked a point (by red cross) in the left panels of Fig. 4 in the unstable regime at $(\tilde{h}^*, \tilde{\tau}) = (2.8, 1.0)$. The corresponding numerical simulations, i.e., the trajectories of vehicles in space-time, are shown in Fig. 5. The system is initialized at equilibrium except one vehicle whose headway and velocity are slightly reduced. (The initial functions $h_n(t), v_n(t)$ are considered to be constant along the interval $t \in [-\tau, 0]$.) The system is integrated by applying 4th order Adam-Bashforth method in Matlab using the step size $\tau/100$. The (rescaled) position of the front bumper $\tilde{x}_n$ of each vehicle is plotted as a function of (rescaled) time $\tilde{t}$. Periodic boundary conditions are considered (ring-road configuration) and the rescaled car-length $\tilde{\ell} = 1$ is used.

One may observe that the patterns appearing after transients are different for human and robotic drivers. For human drivers, although short-wavelength oscillations show up originally, the asymptotic pattern is a long-wavelength traveling wave, i.e., stop-and-go traffic jams appear. In contrast, for robotic drivers the asymptotic pattern consists of short-wavelength oscillations. This means that the patterns concluded from the linear analysis show up at the nonlinear level, demonstrating that delays can radically change the arising patterns in a spatially extended complex system. However, we remark that it may be difficult to map the full nonlinear behavior of the system by using nonlinear simulations only. For example, if the Hopf bifurcations are subcritical one may obtain sustained nonlinear oscillations even on domains where the uniform flow equilibrium is linearly stable [6, 8, 12]. Characterizing the nonlinear dynamics of classes of delayed car-following models is a challenging subject for future research.

CONCLUSIONS

A general class of car-following models was considered and the linear stability of the uniform flow was studied for different (ring-road and platoon) vehicle configurations. It was proven that both configurations give the same stability charts even though the applied mathematical tools are different. It was also shown that when the stability is lost, traveling waves of different wavelength appear. The developing nonlinear waves were demonstrated by numerical simulations. It was shown that the wavelength and frequency of the primary instability depend on the how the delays are incorporated in the systems. The results demonstrate that time delays lead to much more complex behavior than suggested by the zero-delay case. The presented results may lead to better understanding of the dynamics of human-driven vehicle systems and may also allow one to design cooperative autonomous cruise control algorithms for computer-controlled vehicles.

REFERENCES

[1] Helbing, D., 2001. "Traffic and related self-driven many-particle systems". *Reviews of Modern Physics,* **73**(4), pp. 1067–1141.

[2] Nagel, K., Wagner, P., and Woesler, R., 2003. "Still flowing: Approaches to traffic flow and traffic jam modeling". *Operations Research,* **51**(5), pp. 681–710.

[3] Orosz, G., Wilson, R. E., and Stépán, G., 2010. "Traffic jams: dynamics and control". *Philosophical Transactions of the Royal Society A,* **368**(1928), pp. 4455–4479.

[4] Bando, M., Hasebe, K., Nakayama, A., Shibata, A., and Sugiyama, Y., 1995. "Dynamical model of traffic congestion and numerical simulation". *Physical Review E,* **51**(2), pp. 1035–1042.

[5] Davis, L. C., 2003. "Modification of the optimal velocity traffic model to include delay due to driver reaction time". *Physica A,* **319**, pp. 557–567.

[6] Orosz, G., Wilson, R. E., Szalai, R., and Stépán, G., 2009. "Exciting traffic jams: Nonlinear phenomena behind traffic jam formation on highways". *Physical Review E,* **80**(4), p. 046205.

[7] Kesting, A., and Treiber, M., 2008. "How reaction time, update time, and adaptation time influence the stability of traffic flow". *Computer-Aided Civil and Infrastructure Engineering,* **23**(2), pp. 125–137.

[8] Orosz, G., Moehlis, J., and Bullo, F., 2010. "Robotic reactions: Delay-induced patterns in autonomous vehicle systems". *Physical Review E,* **81**(2), p. 025204(R).

[9] Sipahi, R., and Niculescu, S.-I., 2010. "Stability of car following with human memory effects and automatic headway compensation". *Philosophical Transactions of the Royal Society A,* **368**(1928), pp. 4563–4583.

[10] Zhou, J., and Peng, H., 2005. "Range policy of adaptive cruise control vehicles for improved flow stability and string stability". *IEEE Transactions on Intelligent Transportation Systems,* **6**(2), pp. 229–237.

[11] Kurzhanskiy, A. A., and Varaiya, P., 2010. "Active traffic management on freeway networks: a macroscopic approach". *Philosophical Transactions of the Royal Society A,* **368**(1928), pp. 4607–4626.

[12] Orosz, G., and Stépán, G., 2006. "Subcritical Hopf bifurcations in a car-following model with reaction-time delay". *Proceedings of the Royal Society A,* **462**(2073), pp. 2643–2670.

[13] Treiber, M., Hennecke, A., and Helbing, D., 2000. "Congested traffic states in empirical observations and micro-

scopic simulations". *Physical Review E, 62*(2), pp. 1805–1824.

[14] Sugiyama, Y., Fukui, M., Kikuchi, M., Hasebe, K., Nakayama, A., Nishinari, K., Tadaki, S., and Yukawa, S., 2008. "Traffic jams without bottlenecks – experimental evidence for the physical mechanism of the formation of a jam". *New Journal of Physics, 10*, p. 033001.

[15] Swaroop, D., Hedrick, J. K., Chien, C. C., and Ioannou, P. A., 1994. "A comparision of spacing and headway control laws for automatically controlled vehicles". *Vehicle System Dynamics, 23*(8), pp. 597–625.

[16] Gasser, I., Sirito, G., and Werner, B., 2004. "Bifurcation analysis of a class of 'car-following' traffic models". *Physica D, 197*(3-4), pp. 222–241.